Preprints of the 21st IFAC World Congress (Virtual)
Berlin, Germany, July 12-17, 2020

Wake symmetrization of a bluff Ahmed body based on sliding mode control ⋆

K. Mariette * **É. Bideaux** * **F. Bribiesca-Argomedo** *
D. Ébérard * **S. Sesmat** * **Y. Haffner** ** **J. Borée** **
T. Castelain *** **M. Michard** ****

* *Univ Lyon, INSA Lyon, Université Claude Bernard Lyon I, École Centrale de Lyon, CNRS, Ampère UMR5005, Villeurbanne, France (e-mail: kevin.mariette@insa-lyon.fr)*
** *Institut Pprime UPR3346, CNRS, ENSMA, Université de Poitiers, Futuroscope-Chasseneuil, France*
*** *Univ Lyon, Université Claude Bernard Lyon I, École Centrale de Lyon, INSA Lyon, CNRS, LMFA UMR5509, Villeurbanne, France*
**** *Université de Lyon, École Centrale de Lyon, LMFA UMR5509, Ecully, France*

Abstract: Aerodynamic drag reduction is needed to develop future fuel efficient ground transportation vehicles. Our study targets bluff bodies with wake asymmetries due to natural bistability or cross wind contributing to the drag increase at high velocities. The originality of this work is to apply closed loop control techniques based on sliding mode control theory and a Smith like predictor scheme for delay compensation in order to force the wake symmetry. This non linear controller was tuned thanks to experimental study of pulsed jet actuators placed at the back of a modified Ahmed bluff body and shows that wake symmetrization can be achieved either in aligned or cross wind configurations.

Keywords: Fluid flow control, crosswind, sliding mode control, delay compensation.

1. INTRODUCTION

For the sector of road transport, saving energy is a critical issue. At high velocity, the aerodynamic drag is the main contributor to the vehicle fuel and energy consumption. Most of this force comes from the pressure loss at the back of the vehicles (Wood (2003)) generating a large recirculation region (RcRg). Then, by modifying the shear layers structures at the boundaries of the RcRg, the pressure levels on a vehicle base can be influenced by control devices, as in Barros et al. (2016). Hence, many studies on drag reduction focus on passive (curved surfaces, flaps, cavities) (Englar (2005)) and active open-loop control strategies (air jets, active flaps) (Bideaux et al. (2011)) in order to increase the pressure in the RcRg. For example, El-Alti (2012) showed 39% of base pressure improvement with continuous air jets on a truck mock-up. Recently, closed-loop control have shown encouraging results (Plumejeau et al. (2019)) because of promising robustness and adaptability. However, applications of closed-loop approaches still remain difficult to implement on real conditions because of the lack of reliable flow models.

A particular drag reduction strategy for bluff bodies consists in the conservation of the wake symmetry. Indeed, the pressure in the wake is non homogeneous and asymmetries can increase the pressure drag by 4 to 8% (Grandemange et al. (2012)). The base pressure asymmetries can have different origins: a cross wind on the vehicle or, for aligned wind flow, natural bistability in the wake.

Hence, symmetry enforcement methods have been previously employed on bluff bodies in order to obtain additional drag reduction. For example, Brackston et al. (2016) used movable flaps with a predictive closed loop model leading to a net drag reduction of 2% ; Li et al. (2016) worked with pulsed jets at 200 Hz on the bistable wake to symmetrize the pressure gradients with a pressure raise of 2%. Finally, Plumejeau et al. (2019) proposed a model-free closed-loop control of the wake asymmetries thanks to drift-force feedback with air knives blowers and showed 2.5% drag reduction. In the continuity of such experimental studies, this paper focuses on the improvement of wake symmetry thanks to closed-loop control of the centre of pressure (CoP) on a bluff vehicle mock-up backward face. We use high frequency pulsed air jets and a sliding mode control approach which only requires surface pressure measurements.

In Section 2, we present the experimental set up before describing, in Section 3, the behaviours of the CoP subjected to bistability and under open-loop actuation. Finally, Section 4 presents the sliding mode control and ends with the results of the wake symmetry control for different cross wind directions.

⋆ Founded by the French ANR, Activ'Road (Ampre laboratory (INSA, Lyon), P' Institute (ENSMA, Poitiers), LMFA (ECL, Lyon), PSA & Renault Trucks companies)

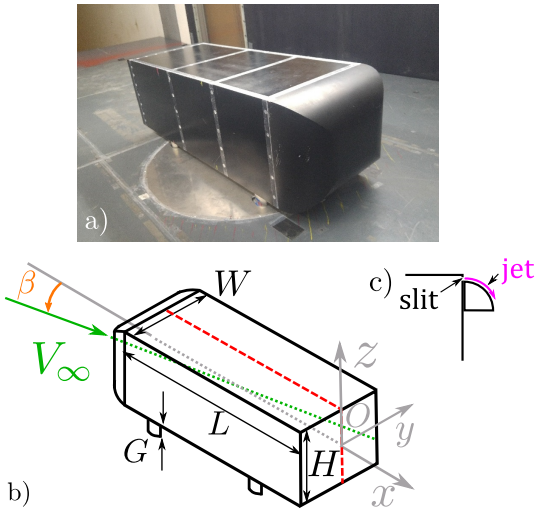

Fig. 1. The experimental mock-up: a) Front view ; b) Back view (schematic) with symmetry plan location (– –), the flow velocity direction (⟶) and mock-up dimension parameters ; c) Close up view of the Coanda surfaces deviating the actuation jets.

2. EXPERIMENTAL SET-UP

In this experimental study, we use a modified *Ahmed body* mock-up model (Ahmed et al. (1984)) with a straight backward face, called the base. Fig. 1 and Table 1 present this mock-up shape and dimensions. The present bluff profile allows the conversion of the mock-up from a cars-like shape to a trailer truck shape by a simple rotation 90° around the x-axis. The base of the mock-up (see Fig. 2.b) is equipped with 35 low-bandwidth sensors and 12 fast transducers, with respective bandwidths of 200 Hz and 2 kHz, providing average values of pressure levels as well as fast fluctuations useful for closed-loop control. We use, as pressure level indicator, the mean pressure ratio γ_p defined as the ratio between the mean pressure value when the control is activated, and the pressure without control. We define analogously the drag force ratio, γ_{C_x} from the controlled an uncontrolled *drag coefficient* C_x:

$$C_x = {}^{F_x}/_{\frac{1}{2}\rho S V_\infty^2} \qquad (1)$$

where F_x is the drag force, ρ the air density at the wind tunnel temperature, V_∞ the flow velocity, and S the cross section of the body relative to the x-direction.

Table 1. Experimental mock-up dimensions

Length	$L = 1.00\,\text{m}$
Width	$W = 0.36\,\text{m}$
Height	$H = 0.30\,\text{m}$
Gap under body clearance	$G = 0.05\,\text{m}$

The mock-up is placed on a raised floor in a closed-loop wind tunnel (ENSMA, Poitiers, France) in order to recreate an homogeneous flow around it. This wind tunnel can generate wind velocities up to 60 m/s and create a fully turbulent flow around the experimental body with a Reynolds number Re about 10^5.

As shown in Fig. 2.c), the supply pressure [1] P_i (②) is kept constant thanks to a PID controller in an upstream tank placed inside the Ahmed body (see Fig. 2.a). This pressurized air passes through 14 ON/OFF valves (③) connected to 26 diffusion slits [2] to generate pulsed jets (④). The slits are distributed all around the edges of the base as described in Fig. 2.b). All the valves on the same edge share a single control signal consisting of a variable-frequency square TTL signal (VFSS) computed by a dSpace rapid prototyping system at a sampling frequency of 4 kHz. In summary, the computed control signal defines the edges to be activated, the frequency of the opening an closing of the valves on each activated edge, and the target tank pressure P_i. The duty cycle of the VFSS can also be included in the command vector but its variation is limited at high frequencies due to opening/closing times of the valves. Here, the duty cycle is fixed at 0.5. The actuation set-up allows to explore jet frequencies up to 1 kHz and maximum jet velocities up to 80 m/s at a supply pressure of 0.4 MPa. These jets are deviated toward the low pressure region by additional curved surfaces, called *coanda surfaces* (see Fig. 1.c), placed below the diffusion slits as proposed by Barros et al. (2016) or Haffner (2018), in order to increase the impact of the pulsed jets on the wake.

Finally a 6-axes aerodynamic balance gives access to the forces acting on the Ahmed body. This balance is linked to the body reference frame and implemented on a pole that enables rotations around the z-direction. The rotation angle β is referenced to an orientation corresponding to an aligned flow with the x-direction along the mock-up (see Fig. 1.b). Hereafter, the lengths are normalized by the height H and the control only use the left and right edges on the base.

[1] expressed *relatively* to the atmospheric pressure

[2] slit dimensions are $1 \times 40\,\text{mm}^2$

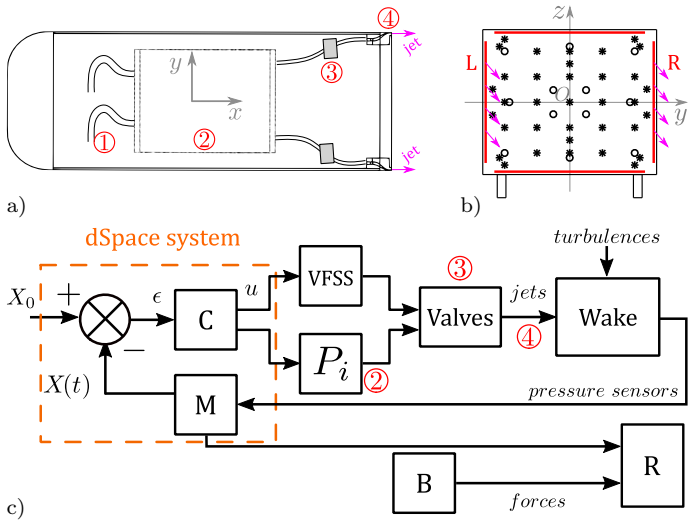

Fig. 2. a) Top-view of the mock-up : ① air supply, ② pressure tank , ③ ON/OFF valves, ④ diffusers ; b) Sensor locations: Fast (2 kHz) ∘ ; Static (200 Hz) ∗ ; and slits for air jet output (—) viewed from the rear. (L) and (R) give the convention for the left and right sides ; c) Block diagram of the control and recordings of the experiment with references to the physical elements in a): the control block **C** regulates the tank supply pressure P_i and generates the activation signal for the ON/OFF (**Valves**) valves pulsing jets into the wake. The pressure signals are treated in **M** before being recorded (in **R**) with the forces collected by the balance **B**. The box (– –) indicates the parts implemented in a dSpace rapid prototyping system.

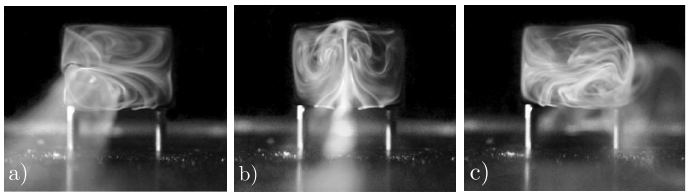

Fig. 3. The bistability : a) Left positioned wake ; b) Transition ; c) Right positioned wake (Grandemange et al. (2012))

3. FEATURES OF THE CENTRE OF PRESSURE

3.1 Natural bistability and forced transition through open-loop control

In this paper, the symmetry of the wake is described by the y-coordinate of the CoP on the base which is taken as the state of the controlled system, and noted X. X is a time varying value and is computed from the 12 fast pressure sensors measurements, p_k, and y-positions, y_k from:

$$X(t) = \frac{\sum_{k=1}^{12} p_k(t) y_k}{\sum_{k=1}^{12} p_k} \tag{2}$$

As shown in Fig. 3 Grandemange et al. (2012), for a natural aligned flow, the bistability induces an important loss of symmetry of the bluff body's wake. A low pressure area, from where the wake develops, can jump randomly from one fixed position to its mirrored position. For an aligned flow at $V_\infty = 35\,\mathrm{m/s}$, with the experimental mock-up body, such bistable transitions occur and are illustrated in the middle of Fig. 4. The left part (negative time) consists of the uncontrolled time series of X and exhibits two possible states of equilibrium where the CoP is stuck most of the time. These uncontrolled bistable positions are better depicted by the power density function of X (PDF_X) on the left part of Fig. 4: two maxima exist in symmetric positions relatively to $y = 0$. We call *deviation from 0*, noted d_X the absolute position of the maxima of the PDF_X curve:

$$d_X = \{y \;/\; PDF_X(y) = max(|PDF_X|)\} \tag{3}$$

For the uncontrolled case, the natural deviation from 0 is:

$$d_{X,\,nat} = 0.046 \tag{4}$$

Next, on the right part of Fig. 4, we activate the right edge of the base and trigger a forced transition of the wake from left ($X < 0$) to right ($X > 0$). We use pulsed jets at a frequency of 1050 Hz on the right edge with a supply pressure $P_i = 0.25\,\mathrm{MPa}$ which results in the CoP being moved to the right and locked at the right asymmetric equilibrium (see Fig. 4 on the rightmost graph). We denote this control signal: $u = +1$.

The symmetric behaviour is observed for the actuation on the left side denoted: $u = -1$. Table 2 summarizes the symmetry parameters obtained for the asymmetric control and the natural flow over longer time periods.

3.2 Frequency effects

Thanks to the previous open-loop tests of CoP displacement, we tested successive forced lateral transitions with alternating left and right edge activation. The actuation frequency was set to 975 Hz, the supply pressure to $P_i = 0.27\,\mathrm{MPa}$ and the flow velocity V_∞ to $25\,\mathrm{m/s}$. Here the control is a low-frequency modulating signal f_m that defines the time of actuation for each side. In Fig. 5, we selected representative results of three different modulation frequencies leading to distinct regimes for the wake:

a) Under-actuated ($f_m = 4\,\mathrm{Hz}$): according to the activated side, X moves towards the left or the right unstable equilibrium position ;
b) Resonant ($f_m = 16\,\mathrm{Hz}$): X oscillates between the two unstable equilibrium positions without reaching a steady state. The time $1/f_m$ is close to *twice* the characteristic transition time for the actuated wake ;
c) Over-actuated ($f_m = 54\,\mathrm{Hz}$): X shows smaller fluctuation magnitudes but its average value is not 0: this open-loop control does not improve the wake asymmetry, even in average.

Open-loop switching could not comply with the objective of wake symmetrization and drag reduction. Indeed, at high frequency, the average value of X did not tend to $y = 0$; on the other hand, small values of f_m created bistable states with transitions observed also in the case of forced transition as in the inclusion of Fig. 4. For the resonant configuration, even though we are able to centre the CoP on average without generating nonsymmetric static states, it generated harmonic oscillations of the wake at a rate corresponding to the *vortex shedding* frequency. The vortex shedding is characterised by low pressure states and vortex generation behind the body. This instability is not desirable since it increases drag and generates vibrations (Roshko (1993)). Although not displayed here, the actuation at high frequencies of the L and R edges (or

Table 2. Symmetry indicators for the uncontrolled ($u = 0$) and one side actuated cases ($u = \pm 1$).

	$u = 0$	$u = +1$	$u = -1$
$\overline{X}$	0.003	0.045	-0.045
σ	0.047	0.016	0.015
d_X	0.046	0.046	0.044

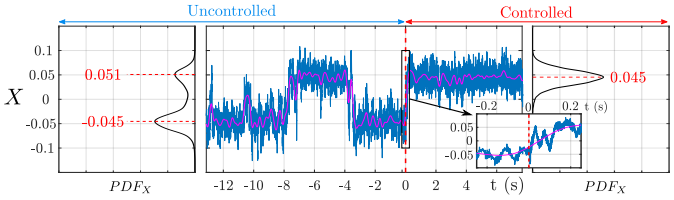

Fig. 4. Time series of the triggered transition of X for $u = +1$ and PDF_X for the uncontrolled and actuated states. A close-up view of the transition (black rectangle) is displayed at the right bottom of the main Fig.. The colour correspond to: (——) raw signal ; (——) 2 Hz filtered data; (– –) control start.

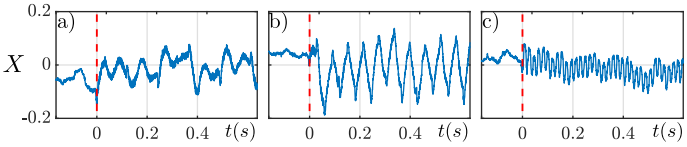

Fig. 5. Open-loop control locations for X for alternated forced transitions at a low frequency f_m (from left to right: $f_m = 4\,\mathrm{Hz}$, 16 Hz, 54 Hz). Control starts at the red dashed lines.

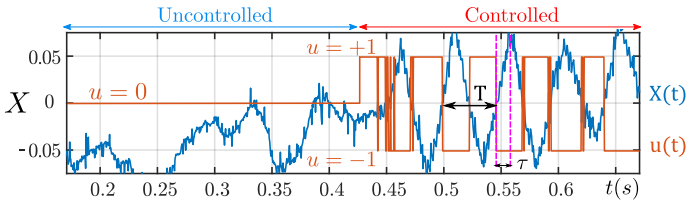

Fig. 6. Time series of X actuated by the SMC Law_1. Identification of an oscillating period T and a delay τ.

of the four edges at the same time) does not really control efficiently the CoP horizontal position. Even though these actuation profile can impact positively the pressure in the RcRg, the wake is still bistable. As a conclusion, this section showed the limitations of open-loop switching actuation for the regulation of X towards 0.

4. CLOSED LOOP CONTROL BY SLIDING MODE

4.1 Sliding mode control: Law_1

Based on these remarks, the second step of this study explored closed-loop control approaches. A sliding mode control (SMC) was chosen here since this technique may provide good robustness even with highly non linear systems. The SMC consists in driving a given system towards a chosen trajectory, called the sliding surface, as fast as possible and then maintaining the system on this trajectory by adjusting its deviations in real time (Slotine (1984)). This regulation technique is particularly suitable for the present experimental system because of the discontinuous nature of the pulsed jets and the finite number of stable positions for the CoP (Utkin (1992)).

First, the control was designed to reduce the error

$$\epsilon = X_0 - X, \tag{5}$$

where $X_0 = 0$ is the desired value for the CoP lateral position. The command $u(\epsilon)$ determines the edge to be activated according to:

$$u(\epsilon) = \begin{cases} -1 \ if \ \epsilon < 0 \\ 0 \ \ if \ \epsilon = 0 \\ +1 \ if \ \epsilon > 0 \end{cases} \tag{6}$$

In other words, the left edge (resp. the right edge) is activated for $\epsilon < 0$ (resp. for $\epsilon > 0$). Compared to the open loop case the modulation frequency driving the edge actuation time is not fixed but varies according to the measured deviation sign.

This SMC law (Law_1) was tested experimentally on the Ahmed body under aligned flow condition with a constant flow velocity $V_\infty = 35$ m/s and a jet actuation frequency of 1050 Hz at a P_i value of 0.2 MPa. In Fig. 6 we can observe that the command u switches from left actuation ($u < 0$) to right actuation ($u > 0$) according to the sign of X, and by doing so, it suppresses the bistable states. However, a resonant behaviour appears with an excitation frequency of 23 Hz, close to the vortex shedding frequency (around 18 Hz at $V_\infty = 35$ m/s). At the same time, the pressure in the RcRg drops dramatically.

In conclusion, with the SMC Law_1, the actuation switches according to the sign of ϵ but, unfortunately, the control acts with a delay on the CoP position. Even if the bistability was suppressed, the SMC Law_1 could not increase the base pressure nor decrease the drag because of the vortex shedding excitation.

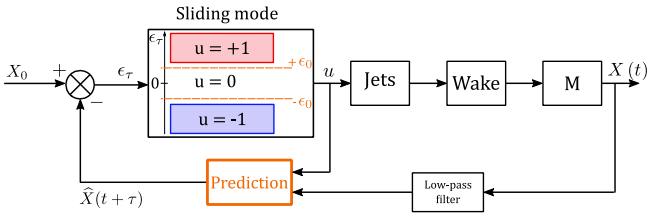

Fig. 7. Block diagram of the SMC laws 2 and 3 including the Smith predictor and a dead-band $[-\epsilon_0\ ,\ +\epsilon_0]$ around $X_0 = 0$. For the SMC Law_2, $\epsilon_0 = 0$.

4.2 Sliding mode based on a prediction: Law_2

Referring again to Fig. 6, we used the observation of the signal shapes of the measured output $X(t)$ and the applied command $u(t)$ to improve the SMC. The quasi-square input u is converted to triangular fluctuations like an integrator would do, but with a $+\frac{\pi}{4}$ phase shift. Thanks to this observation we used a simple integrator model and built a delay compensator similar to a Smith predictor (Normey-Rico (2007)). The objective was to perform an adjusted SMC, the SMC Law_2, without exciting turbulent instabilities as the vortex shedding.

The identified model is as follow:

$$\dot{X}(t) = Ku(t-\tau) \tag{7}$$

where

- $\dot{X}$ expresses the derivation with respect to the time of X
- u is the control signal to the lateral jets
- K corresponds to a speed of transition of X
- τ, the time delay is supposed constant, with $\tau =$ 12 ms (see Fig. 6)

The block diagram in Fig. 7 presents the prediction architecture. X is computed at the time $t+\tau$ in the *Prediction* block based on the applied control during τ by:

$$\widehat{X}(t+\tau) = X(t) + \int_0^\tau Ku(t-\tau+r)\,dr \tag{8}$$

Then the new error is evaluated by:

$$\epsilon_\tau = X_0 - \widehat{X}(t+\tau) \tag{9}$$

Using the same test configuration as in Section 4.1, the SMC laws 1 and 2 were compared. Fig. 8 shows the values of the pressure ratio γ_p recorded by five pressure sensors on the middle line ($z = 0$) of the base (see Fig. 2.b) as a function of time. Three test were performed sequentially:

① Uncontrolled flow, natural bistable wake ;
② SMC Law_1 without compensation of the delay ;
③ SMC Law_2 with Smith predictor compensating the delay (see Fig. 7).

As stated before, for the SMC Law_1, in part ②, the CoP was no longer bistable but important pressure decreases were observed (darkest blue patches in Fig. 8, part ②). In comparison, for the SMC Law_2 in part ③, the pressure levels displayed are higher. The difference of shade colours

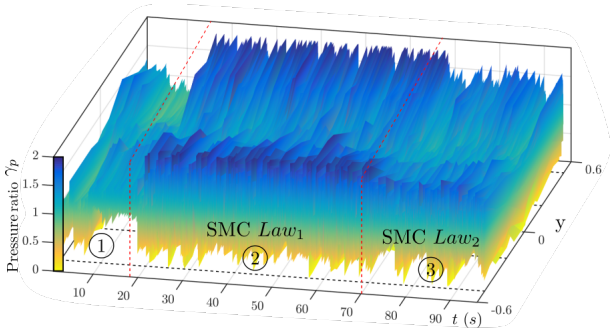

Fig. 8. Pressure ratio levels: ① bistable pressure states, ② pressure levels for the SMC Law_1, ③ delay compensation scheme. The red dashed lines separate the control parts.

between ② and ③ shows the positive effects of the delay predictor on the pressure.

Nevertheless, the delay compensation generates important chattering effects and decreases the performance of the SMC Law_2 control performances.

4.3 Effects of wake symmetry forcing: SMC Law_3

To counter the chattering, a *dead-band* around the objective value of $X_0 = 0$ was defined. For values of $\widehat{X}$ inside the dead-band, the control was stopped (El Makrini et al. (2016)). This dead-band is parametrized by ϵ_0 and the control Law_2 is modified to the SMC Law_3 with:

$$u(\epsilon_\tau) = \begin{cases} -1 \ if \ \epsilon_\tau < -\epsilon_0 \\ 0 \ \ if \ |\epsilon_\tau| < \epsilon_0 \\ +1 \ if \ \epsilon_\tau > \epsilon_0 \end{cases} \quad (10)$$

Basically, the SMC Law_3 uses $\epsilon_0 > 0$ and its structure is also described by the block diagram 7. Results obtained with the SMC Law_3 including the dead-band, for $\epsilon_0 = 0.8 \times d_{X,nat} = 0.0370$, jets frequency of 1050 Hz, supply pressure of 0.2 MPa and $V_\infty = 35$ m/s are presented in Fig. 9. The upper part a) presents the time series of X with and without control. With the SMC Law_3, the bistable states have disappeared and the associated PDF graph at the right proves the control to be efficient in terms of symmetry compared to the natural PDF_X at the left. In the controlled configuration, the deviation from 0, d_X, was reduced by 94.2% with respect to the uncontrolled case and the standard deviation of X was reduced by 35.3%.

The lower part b) is a close up view of the upper time series at the control activation time showing when the control activates (positives and negatives orange peaks). The brief activations are enough to re-centre X and, the rest of the time, the control is stopped. The CoP stays around the unstable symmetric state: $X = 0$.

Whereas the control is always activated (positively or negatively) with the SMC Law_2 (Fig. 6), the dead-zone removes the bistability without enhancing the vortex shedding and at a low energetic cost. This sparse actuation led to the reduction of the bistability and slight modifications of the drag as shown in Table 3. It shows, for different pressures P_i, the variation Δ (in %) of the pressure ratio γ_p, the drag force ratio γ_{C_x}, and the symmetry parameters for X: $\overline{X}$, σ and d_X. These variations are computed relatively to the uncontrolled cases and every negative value corresponds to a diminution of the associated parameter.

Table 3. Effects of the SMC Law_3 for different tank pressure P_i on the pressure, drag ratio and symmetry parameters.

P_i [MPa]	$\Delta\gamma_p$ [%]	$\Delta\gamma_{C_x}$ [%]	$\lvert\overline{X}\rvert$	σ	d_X
0.25	+1.73	+2.15	3.10^{-4}	0.031	0.008
0.24	+1.25	+1.73	7.10^{-5}	0.030	0.006
0.23	+0.34	+1.14	6.10^{-4}	0.030	0.002
0.22	−0.78	+0.59	5.10^{-4}	0.031	0.003
0.21	−0.89	+0.53	3.10^{-4}	0.031	0.004
0.20	−1.41	+0.09	4.10^{-4}	0.030	0.002
0.19	−2.11	−0.11	2.10^{-4}	0.031	0.007
0.18	−2.03	−0.19	1.10^{-4}	0.031	0.006

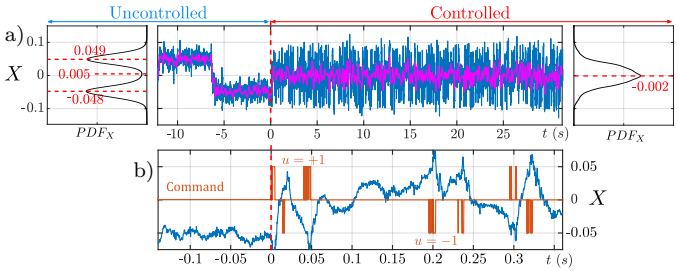

Fig. 9. a) Time series for the evolution of X whith the SMC Law_3 (see Fig. 7) and PDF graphs associated to the uncontrolled and controlled cases ; b) close up view at the control activation.

From the symmetry point of view, the SMC Law_3 impacts positively the CoP lateral location. The mean value is maintained close to 0 while d_X is centred in comparison to the data in table 2. Within the range of tested supply pressures, the best gain for the drag ratio is obtained for a supply pressure $P_i = 0.18$ MPa, where the pressure ratio decreased by 2%. The drag force ratio kept decreasing with the reduction of P_i and it seems that lower supply pressure for the jets could have generated clear drag gains.

Although the two ratios show the same variation with the reduction of pressure supply P_i, obtaining negative pressure ratio is not sufficient for net drag reduction. Studies, as in Szmigiel (2017), show that jets create a localised loss of pressure on the base edges surfaces. It is possible that our operating configurations generated sufficient jets for pressure raise but also significant body forces which reduced the net drag gains.

4.4 Application to crosswind configurations

Up to here, our experiments were conducted with the mock-up aligned with respect to the wind direction. Based on the previous results, the SMC was applied to the mock-up in a drift configuration. This configuration is characteristic of a vehicle direction change or non aligned wind. The drift is parametrized by the yaw angle β (see Fig. 1.b) and can be monitored during the experiment with a small amplitude of $\pm 1.7\,°$. It has been verified that this drift is able to create a fully non-symmetric static wake.

The SMC Law_3 has been applied in different drift configurations in order to evaluate its capacity to maintain a symmetric wake in nonsymmetric flow conditions. The results presented in Table 4 are obtained with a jet frequency of 1050 Hz, a supply pressure $P_i = 2.5 \times 10^5$ Pa, and $V_\infty = 35$ m/s. As displayed, for this important pressure, no improvements in terms of pressure nor drag are achieved for small drift angle or for the aligned configuration. How-

β [°]	**Uncontrolled**			**SMC** Law_3				
	$\overline{X}$	σ	d_X	$\Delta\gamma_p$ [%]	$\Delta\gamma_{C_x}$ [%]	$\lvert\overline{X}\rvert$	σ	d_X
-0.7	-0.042	0.025	0.049	+0.53	+2.23	0.001	0.030	0.012
0	0.003	0.047	0.046	+1.73	+1.71	0.001	0.030	0.008
+1.7	0.044	0.014	0.044	-2.95	-1.70	0.012	0.029	0.020

Table 4. Symmetry parameters $\overline{X}$, σ, d_X with the pressure and drag ratio variations (respectively $\Delta\gamma_p$ and $\Delta\gamma_{C_x}$) expressed in % for different yaw angles β with the SMC Law_3.

ever, for the configuration with a higher drift angle of $\beta = 1.7°$, a drag reduction of 1.70% and a pressure raise of 3% are observed.

Even though, for the strongest drifts, the CoP position is only re-centred by 48.5%, the impact on the shear layers is visible on the wake pressure and on the drag values. On the other hand, in the case of small angles or $\beta = 0$, the jets strength is too large to produce a pressure raise up as seen in Table 3. Referring to the results of Tables 3 and 4, a lower tank pressure could be used for small drift angle while higher values of P_i could be required under important crosswind conditions. Therefore the development of SMC for wake symmetry with adapted supply pressure with the measurement of the wind direction could be an effective way of reducing drag with a reduced energy cost.

5. CONCLUSION

The previous developments have presented the effects of asymmetries and their control on aerodynamic drag of bluff bodies. The nonsymmetric states of the wake of an Ahmed body with straight back were investigated to develop an active control based on pulsed air jets at the lateral edges of the body's backward face. The implemented sliding mode control on the centre of pressure lateral position was successful for symmetry preservation in aligned configuration but presented important drawbacks in terms of pressure in the wake. The control was improved by a delay compensation Smith like predictor and a deadband domain around the desired centred position. For an aligned vehicle mock-up, it largely reduced the bistability and efficiently rose the pressure level by 2% but no significant drag gain were concomitantly recorded. However, evidences of relation between jet strength and drag force were observed. With a further reduction of the jet strength, we believe that the proposed sliding mode control and its sparse actuation could lead to net drag reductions.

Finally the control was used on an unaligned configuration to test its effects in case of cross wind on the body. In this last case, we obtained interesting gains in term of pressure and drag, respectively of 3% and 1.7% with a drift angle of 1.7°. While the employed jets were too powerful for net drag reduction in the aligned and nearly aligned configurations, highly energetic jets could be used in the case of important cross wind. Therefore, in real situation where wind surges can appear suddenly, our closed-loop control approach with adapted jets forces could mitigate efficiently the drag.

REFERENCES

Ahmed, S.R., Ramm, G., and Faltin, G. (1984). Some Salient Features Of The Time-Averaged Ground Vehicle Wake. *SAE Technical Paper Series*.

Barros, D., Borée, J., Noack, B.R., Spohn, A., and Ruiz, T. (2016). Bluff body drag manipulation using pulsed jets and Coanda effect. *Journal of Fluid Mechanics*, 805, 422–459.

Bideaux, E., Bobillier, P., Fournier, E., Gillieron, P., Hajem, M.E., Champagne, J.Y., Gilotte, P., and Kourta, A. (2011). Drag reduction by pulsed jets on strongly unstructured wake: towards the square back control. *International Journal of Aerodynamics*, 1(3/4), 282–298.

Brackston, R.D., García de la Cruz, J.M., Wynn, A., Rigas, G., and Morrison, J.F. (2016). Stochastic modelling and feedback control of bistability in a turbulent bluff body wake. *Journal of Fluid Mechanics*, 802.

El-Alti, M. (2012). *Active Flow Control for Drag reduction of Heavy Vehicles*. PhD Thesis, Chalmers university of Technology.

El Makrini, I., Rodriguez Guerrero, C., Lefeber, D., and Vanderborght, B. (2016). The variable boundary layer sliding mode control: A safe and performant control for compliant joint manipulators.

Englar, R.J. (2005). Improved Pneumatic Aerodynamics for Drag Reduction, Fuel Economy, Safety and Stability Increase for Heavy Vehicles.

Grandemange, M., Cadot, O., and Gohlke, M. (2012). Reflectional symmetry breaking of the separated flow over three-dimensional bluff bodies. *Physical Review E*.

Haffner, Y. (2018). Manipulation of 3d blunt body turbulent wakes: drag reduction and wake equilibrium. URL `meetings.aps.org/Meeting/DFD18/Session/A17.9`.

Li, R., Barros, D., Borée, J., Cadot, O., Noack, B.R., and Cordier, L. (2016). Feedback control of bimodal wake dynamics. *Experiments in Fluids*, 57(10).

Normey-Rico, J.E. (2007). *Control of Dead-time Processes*. Advanced Textbooks in Control and Signal Processing. Springer London, London.

Plumejeau, B., Delprat, S., Keirsbulck, L., Lippert, M., and Abassi, W. (2019). Ultra-local model-based control of the square-back Ahmed body wake flow. *Physics of Fluids*, 31, 085103.

Roshko, A. (1993). Free Shear Layers, Base Pressure and Bluff-Body Drag. Technical report, California Inst. of Tech. Pasadena Graduate Aeronautical Labs.

Slotine, J.J.E. (1984). Sliding controller design for nonlinear systems. *International Journal of Control*, 40, 421–434.

Szmigiel, M. (2017). *Effet du flux de soubassement sur la dynamique du sillage d'un corps non profilé à culot droit*. PhD Thesis, Ecole Centrale de Lyon.

Utkin, V.I. (1992). *Sliding Modes in Control and Optimization*. Springer Berlin Heidelberg, Berlin, Heidelberg.

Wood, R. (2003). Aerodynamic Drag and Drag Reduction. In *41st Aerospace Sciences Meeting and Exhibit*. American Institute of Aeronautics and Astronautics, Reno, Nevada.